Additive Manufacturing: Metallurgy, Cut Analysis & Porosity

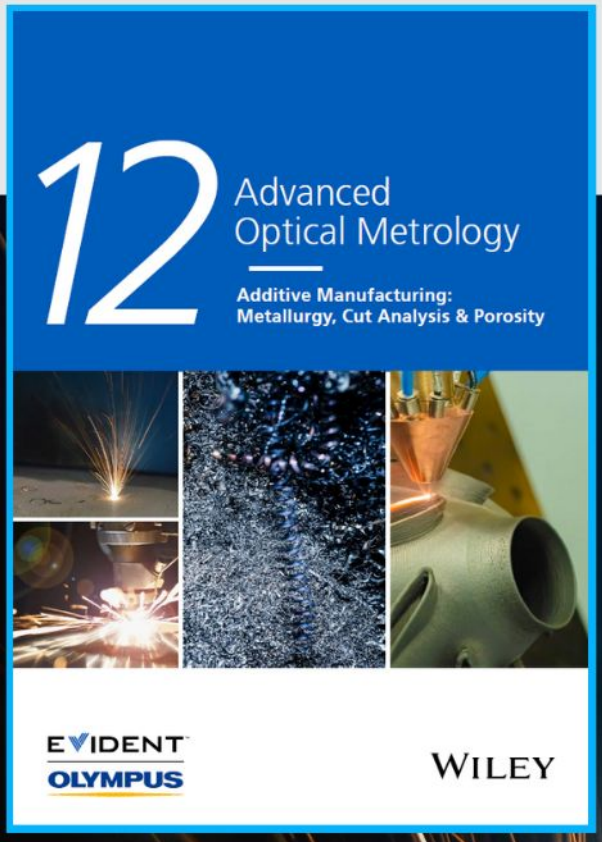

The latest eBook from Advanced Optical Metrology. Download for free.

In industry, sector after sector is moving away from conventional production methods to additive manufacturing, a technology that has been recommended for substantial research investment.

Download the latest eBook to read about the applications, trends, opportunities, and challenges around this process, and how it has been adapted to different industrial sectors.

EVIDENT
OLYMPUS

WILEY

NANO · MICRO small
www.small-journal.com

In-Operando Lithium-Ion Transport Tracking in an All-Solid-State Battery

Takane Kobayashi, Tsuyoshi Ohnishi, Takahiro Osawa, Andrew Pratt, Steve Tear, Susumu Shimoda, Hidetada Baba, Mikko Laitinen, and Timo Sajavaara*

An all-solid-state battery is a secondary battery that is charged and discharged by the transport of lithium ions between positive and negative electrodes. To fully realize the significant benefits of this battery technology, for example, higher energy densities, faster charging times, and safer operation, it is essential to understand how lithium ions are transported and distributed in the battery during operation. However, as the third lightest element, methods for quantitatively analyzing lithium during operation of an all-solid-state device are limited such that real-time tracking of lithium transport has not yet been demonstrated. Here, the authors report that the transport of lithium ions in an all-solid-state battery is quantitatively tracked in near real time by utilizing a high-intensity thermal neutron source and lithium-6 as a tracer in a thermal neutron-induced nuclear reaction. Furthermore, the authors show that the lithium-ion migration mechanism and pathway through the solid electrolyte can be determined by *in-operando* tracking. From these results, the authors suggest that the development of all-solid-state batteries has entered a phase where further advances can be carried out while understanding the transport of lithium ions in the batteries.

1. Introduction

Characterization of the underlying properties of all-solid-state batteries is necessary to fully realize the significant advantages of this battery technology, such as increased energy densities, shorter charging times, and improved safety. To this end, various analytical methods have been applied to probe these properties and provide a better understanding of how they influence operation and performance.[1–3]

All-solid-state batteries are secondary (rechargeable) batteries that charge and discharge by transporting lithium ions between the positive and negative electrodes. For continued development, it is essential to understand how lithium ions are transported and distributed in the battery during operation. However, as the third lightest element, methods for quantitatively analyzing lithium during operation of an all-solid-state device are limited such that real-time tracking of lithium transport has not yet been demonstrated.

Against that background, ion beam analysis[4–11] and $^{6}Li(n,\alpha)^{3}H$ thermal neutron-induced nuclear reactions[12–17] have been used to quantitatively track the transport of lithium ions in all-solid-state battery-related materials to date. However, due to fundamental limitations of these approaches, both methods have only succeeded in analyzing the depth distribution of lithium ions in the battery in specific charged and discharged states,[4–14,17] or in tracking their transport with very poor statistics.[15,16] Ion beam analysis utilizing, for example, the $^{7}Li(p,\alpha)^{4}He$ nuclear reaction and elastic recoil detection, is hampered by a small reaction cross-section[18,19] and large irradiation damage,[11] while using a neutron-induced nuclear reaction faces the obstacles of a low natural abundance of lithium-6 and the small number of high-intensity thermal neutron facilities.[20,21]

Nevertheless, the use of thermal neutrons has the significant advantage that irradiation damage caused by the incident neutron beam is almost negligible allowing an all-solid-state device to be analyzed over extended periods, for example, 1 month, while still functioning as a battery.[12,14] We hypothesized that this feature of the method could be used to track the transport of lithium ions in an all-solid-state battery operating at low charging or discharging rates, for example, 0.01C.

T. Kobayashi, S. Shimoda, H. Baba
RIKEN
the Institute of Physical and Chemical Research
2-1 Hirosawa, Wako, Saitama 351-0198, Japan
E-mail: tkoba@b-star.jp
T. Ohnishi
National Institute for Materials Science (NIMS)
1-1 Namiki, Tsukuba, Ibaraki 305-0044, Japan
T. Osawa
Japan Atomic Energy Agency (JAEA)
2–4 Shirakata, Tokai-mura, Naka-Gun, Ibaraki 319–1195, Japan
A. Pratt, S. Tear
School of Physics, Engineering and Technology
University of York
Heslington, York YO10 5DD, UK
M. Laitinen, T. Sajavaara
Department of Physics
Accelerator Laboratory
University of Jyväskylä
P.O. Box 35, Jyväskylä FI-40014, Finland
The ORCID identification number(s) for the author(s) of this article can be found under https://doi.org/10.1002/smll.202204455.

DOI: 10.1002/smll.202204455

This coincided with the news in Summer 2021 that the Japan Research Reactor-3 (JRR-3)[22,23] was to resume its use for experiments following suspension for over 10 years.[24] Following this resumption, the thermal neutron flux intensity at the JRR-3 prompt gamma-ray analysis (PGA) experimental space was measured to be 1.8×10^8 n cm^{-2} s^{-1}. Prior results obtained in experiments using a thermal neutron flux intensity of 5×10^6 n cm^{-2} s^{-1}, required around 10 h simply to obtain one spectrum with satisfactory statistics.[12] The much higher neutron flux intensity at JRR-3 was therefore estimated to enable the measurement of a comparable spectrum in only 17 min. Moreover, by enriching the isotope ratio of lithium-6 of the raw materials (e.g., $LiCoO_2$ and Li_3PO_4) used for all-solid-state batteries, the concentration of lithium-6 in the batteries could be increased greater than 12 times.[17] By combining JRR-3 with an enriched isotope ratio of lithium-6 in a sample battery, we deduced that the transport of lithium ions in the battery during charging or discharging at a rate of approximately 1C could be tracked.

In the present study, we demonstrate that the transport of lithium ions in an all-solid-state battery ($Pt/LiCoO_2/Li_3PO_4/Ta$) with a lithium-6-enriched positive electrode could be tracked in near real time during charging using JRR-3. Furthermore, by analyzing the transport, it is proposed that lithium ions in the Li_3PO_4 solid electrolyte move via the vacancy migration mechanism with the migration pathway restricted rather than being distributed uniformly over the entire electrolyte area. The tracer only functions as a tracer under limited conditions. Since the configuration of the present sample is not suitable for tracking lithium-ion transport during discharge, this mode of operation is not discussed in this paper.

2. Results and Discussion

2.1. Strategic Sample Preparation for Lithium-Ion Transport Tracking in a Battery

An all-solid-state battery consists of a current collector on the positive electrode side, a positive electrode, a solid electrolyte, a negative electrode, and a current collector on the negative electrode side with the key characteristics of the battery mainly dependent on the solid electrolyte.[25] Considering this fact, using experiments that track lithium ion transport, we investigated whether the migration mechanism of lithium ions in the Li_3PO_4 solid electrolyte used in this study could be clarified. Previous theoretical work suggests that lithium-ion migration takes place through the vacancy migration mechanism[26] in which lithium-ion transport in the solid electrolyte proceeds as follows:

(1) Charging causes some lithium ions in the solid electrolyte near the negative electrode to move to the negative electrode, which creates vacancies in the solid electrolyte on the negative electrode side;
(2) Lithium ions in the solid electrolyte move in sequence to fill the vacancies, and the vacancies move to the positive electrode side;
(3) Lithium ions from the positive electrode move to fill the vacancies created on the positive electrode side of the solid electrolyte;
(4) Lithium-ion transport progresses through repetition of (1)–(3) while charging is taking place.

To illustrate the above mechanism, consider an all-solid-state battery that only incorporates lithium-6 ions. During charging in such a battery, as many lithium-6 ions move from the solid electrolyte to the negative electrode as move from the positive electrode to the solid electrolyte. As a result, there is no net change in the number (isotope ratio) of lithium-6 in the solid electrolyte before compared with after the transport of lithium ions has occurred.

In contrast, when the concentration of lithium-6 in either the positive electrode or the solid electrolyte is enriched, the total number of lithium-6 ions in the solid electrolyte would change if lithium-ion transport occurs via the vacancy migration mechanism. That is, when the lithium in the positive electrode is predominantly lithium-6 and the lithium in the solid electrolyte is predominantly lithium-7, some lithium-7 ions contained in the solid electrolyte move to the negative electrode by charging, and an equal number of lithium-6 ions are transported from the positive electrode to the solid electrolyte. As a result, the number (isotope ratio) of lithium-6 in the solid electrolyte increases.

Moreover, when the lithium content in the solid electrolyte and positive electrode is predominantly lithium-6 and lithium-7, respectively, charging causes the transport of some lithium-6 ions contained in the solid electrolyte to the negative electrode with an equal number of positive electrode lithium-7 ions transported to the solid electrolyte. As a result, the number (isotope ratio) of lithium-6 in the solid electrolyte is reduced.

Hence, in both of the above cases, lithium-6 functions as a tracer. In this study, the transport of lithium ions in an all-solid-state battery is tracked by utilizing the first case above which increases the isotope ratio of lithium-6 in the solid electrolyte.

2.2. Lithium-Ion Transport Tracking in an All-Solid-State Battery

Figures 1–3 show the spectral changes obtained from the battery before, during, and after charging for a range of individual spectrum acquisition times. S1 **Figure 4** shows the charging curve corresponding to the charging period shown in Figures 1–3.

Figure 1 shows the evolution of the spectra for an acquisition time of 1 min. Figure 1a–d shows, respectively, consecutive spectra obtained over 1 h before charging, during the charging period, for 1 h after charging, and between 1 and 2 h after charging. From this figure, it is found that the transport of lithium ions in the battery during charging has been successfully tracked in near real time although with relatively poor statistics.

As shown in Figure 4, the voltage between terminals reached 4.2 V during charging. This fact indicates that charging caused the precipitation of lithium on the negative electrode side.[17,27] Nevertheless, no significant spectral peak of lithium-6 on the negative electrode after charging was observed. In addition, an increase in lithium-6 in the solid electrolyte has clearly occurred during charging. From these results, the transport indicates that lithium ions in the solid electrolyte, which mostly consists of lithium-7, were transported to the negative electrode, and

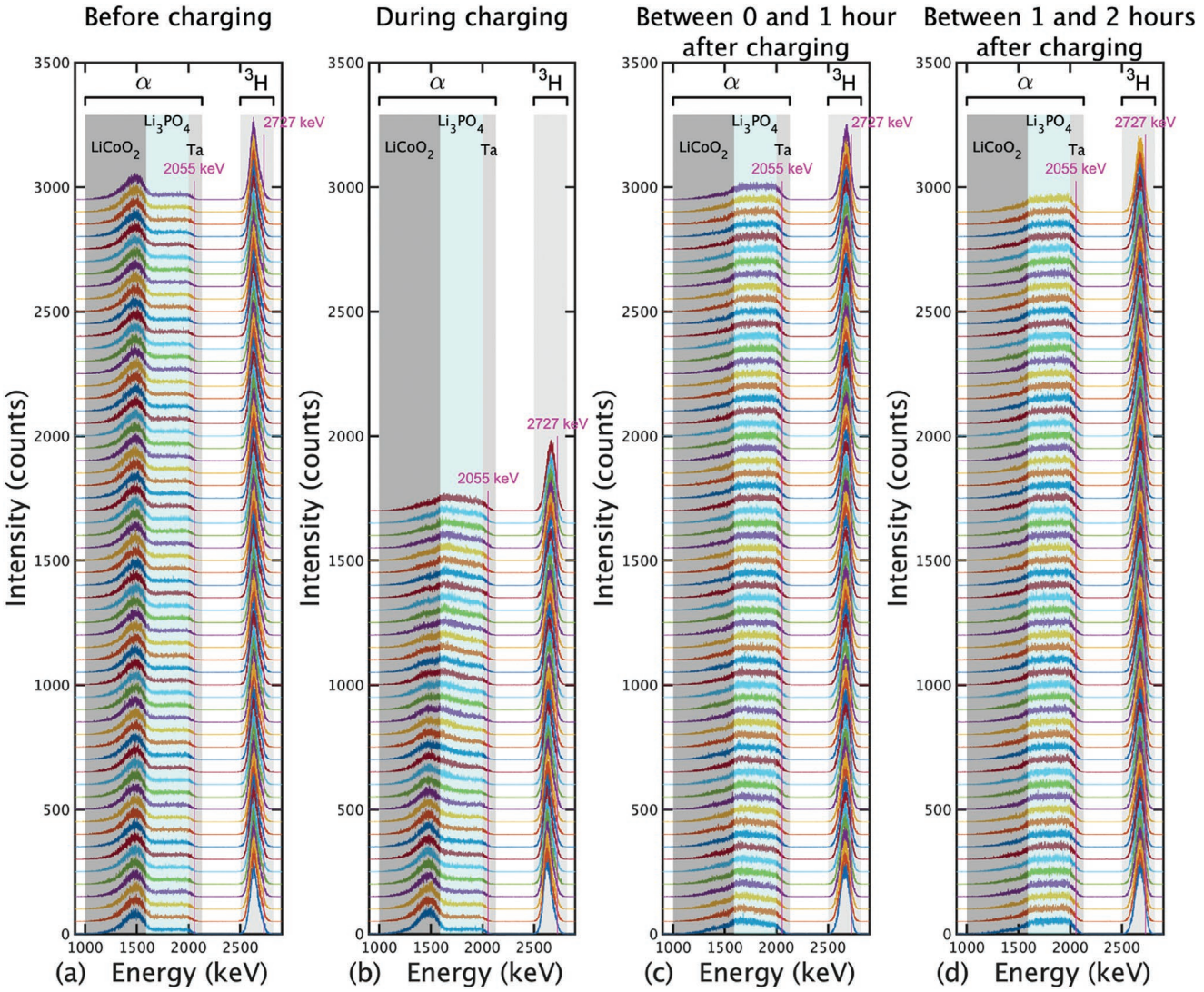

Figure 1. Energy spectra obtained consecutively for an acquisition time of 1 min: a) for 1 h before charging, b) during charging, c) for 1 h immediately after charging, and d) between 1 and 2 h after charging. An off-set is applied to distinguish the various spectra and the different regions of the battery are indicated.

lithium ions in the lithium-6 enriched positive electrode were transported to the solid electrolyte. This result is consistent with the transport of lithium ions described in the sample battery preparation strategy outlined above, strongly suggesting that lithium-ion transport occurs via the vacancy migration mechanism.

Figure 2 shows the spectral evolution for an acquisition time of 5 min with the spectra showing improved statistics when compared with a 1-min acquisition time, demonstrating that the transport of lithium ions could be tracked with sufficient precision.

Figure 3 shows spectra where the acquisition time has been increased further still, to a value of 1 h. The blue and red curves in this figure show the spectra before charging and between 1 and 2 h after charging, respectively. Focusing on the red spectrum, although the region corresponding to the solid electrolyte is increasing to the right, it is highly possible that lithium ions are evenly distributed throughout the electrolyte when energy straggling is considered.

Moreover, considering the area ratio of the positive electrode region to the solid electrolyte region and the lithium isotope ratio of each layer in the blue spectrum before charging in Figure 3, it is found that the total number of lithium atoms (ions) in the solid electrolyte layer is several times greater than that in the positive electrode layer. Nevertheless, it is highly possible that lithium ions are distributed almost uniformly across the solid electrolyte after charging which would occur if the ions do not move uniformly across the entire region of the solid electrolyte, but only in a limited region.

2.3. Calculation of the Migration Region of Lithium Ions in the Li_3PO_4 Solid Electrolyte Used

To calculate the migration region of lithium ions in the Li_3PO_4 solid electrolyte, SIMNRA[28,29] has been used for quantitative analysis. Note that the SIMNRA program has been developed

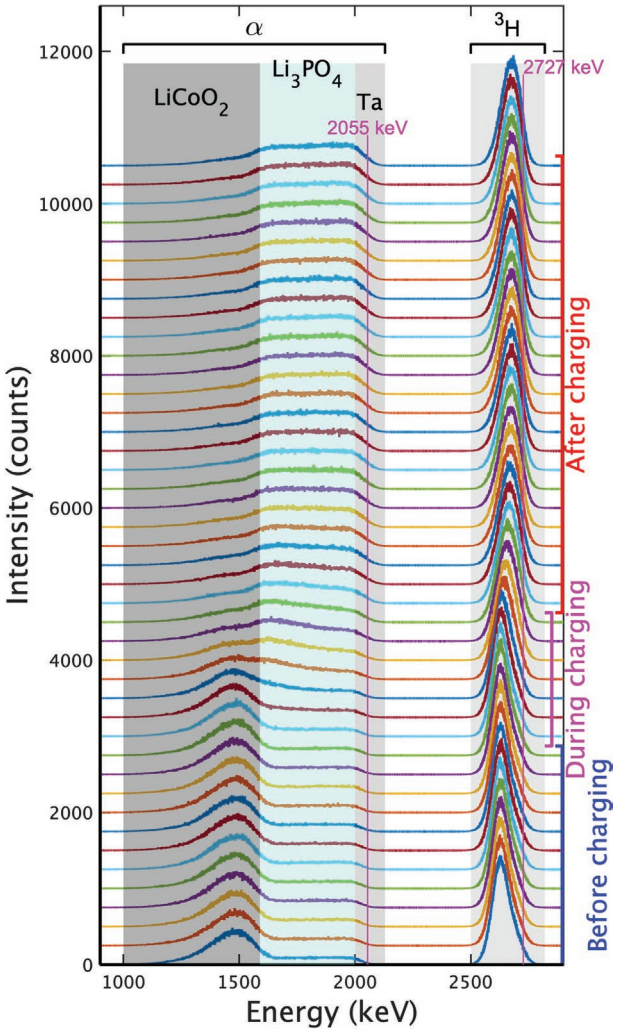

Figure 2. Energy spectra obtained consecutively before, during, and after charging for an acquisition time of 5 min. An off-set is applied to distinguish the various spectra.

for ion beam analysis, and has recently been extended to accommodate thermal neutron-induced nuclear reactions.[29]

In the analysis using SIMNRA, the spectral curve showing the experimental result is indicated by a round marker. As a result, the experimental results appear to be drawn with a wide solid line as shown in **Figures 5** and **6**. In the analyses, the lithium distributions were adjusted until the curves of the simulation results fit within the curves of the experimental results.

The green curve in Figure 5a shows the spectrum obtained before charging as analyzed by SIMNRA, with the blue curve the equivalent experimental spectrum, as presented in Figure 3. The SIMNRA analysis was performed by adjusting the thickness of each component and the roughness of the film of each component in units of 10^{15} atoms cm^{-2}. The reason for varying the roughness of the film is due to the tail in the spectrum on the low-energy side. The roughness referred to here is the nonuniformity of the film thickness deposited on the smooth substrate in units of 10^{15} atoms cm^{-2}.[29] As can be seen from Figure 5, this approach results in good agreement between the experimental and simulated results. **Table 1** summarizes the thickness of the positive electrode layer and solid electrolyte layer as well as the film roughness of each layer as obtained from the analysis. In addition, a schematic of the depth profile of each element of each layer is shown in Figure 5b. From the number of lithium atoms (ions) shown in Table 1, it can be deduced that the total number of lithium atoms (ions) in the solid electrolyte layer before charging is about five times that of the positive electrode layer.

The black curve in Figure 6a shows the result from the SIMNRA analysis after charging with the red curve the experimental result, as presented in Figure 3. This analysis was carried out assuming that no migration other than lithium ions occurred, and that the film roughness remained constant. As for the case before charging in Figure 5, there is good agreement between the experimental and simulated results. These agreements suggest that the assumptions used in the migration models described above are not unrealistic. **Table 2** summarizes the number of lithium atoms (ions) in the positive electrode layer, the isotope ratio of lithium-6 in the solid electrolyte layer, and the number of atoms of precipitated lithium atoms (ions) after charging used in the analysis. In addition, a schematic of the depth profile of each element in each layer is shown in Figure 6b.

Since the number of lithium atoms in each layer and the isotope ratio of lithium-6 before and after charging could be calculated, a simple Monte Carlo simulation has been performed to determine whether lithium-ion transport in the Li_3PO_4 solid electrolyte occurs uniformly over the entire cross-sectional area of the electrolyte or if it is constrained to a limited region. The simulation was carried out by considering that the lithium-ion migration mechanism is a vacancy migration mechanism, the ratio of the total number of lithium atoms (ions) in the positive electrode layer and the solid electrolyte layer, and the isotope ratio of lithium-6 in each layer. The results are shown in **Figure 7**. In addition, the simulation has been performed assuming that the ratio of the transport region when lithium-ion movement is considered to be constrained to a particular channel is 0.2.

The reason for setting the ratio of the transport region to 0.2 is as follows. As mentioned before, when a lithium ion moves by the vacancy migration mechanism during charging, a lithium ion from the solid electrolyte on the negative electrode side moves to the negative electrode, and a vacancy is generated in the solid electrolyte on the negative electrode side. A lithium ion moves in sequence to fill the vacancy, and finally the vacancy moves to the solid electrolyte on the positive electrode side. The vacancy is filled with a lithium ion from the positive electrode. As a result, the lithium ions of the solid electrolyte are replaced by the lithium ions from the positive electrode. As a result of the experiment, the lithium ions in the replaced solid electrolyte are uniformly distributed in the depth direction. Since the total number of lithium ions in the solid electrolyte before charging is five times as large as the total number of lithium ions in the positive electrode, it is reasonable to assume that the ratio of lithium-ion transport regions in the solid electrolyte is less than 0.2 (= 1/5).

The distribution of lithium ions before charging used in the simulation is indicated in Figure 7a. Figure 7b,c shows the simulation results for a uniform migration model and a selected area migration model after charging, respectively. In addition,

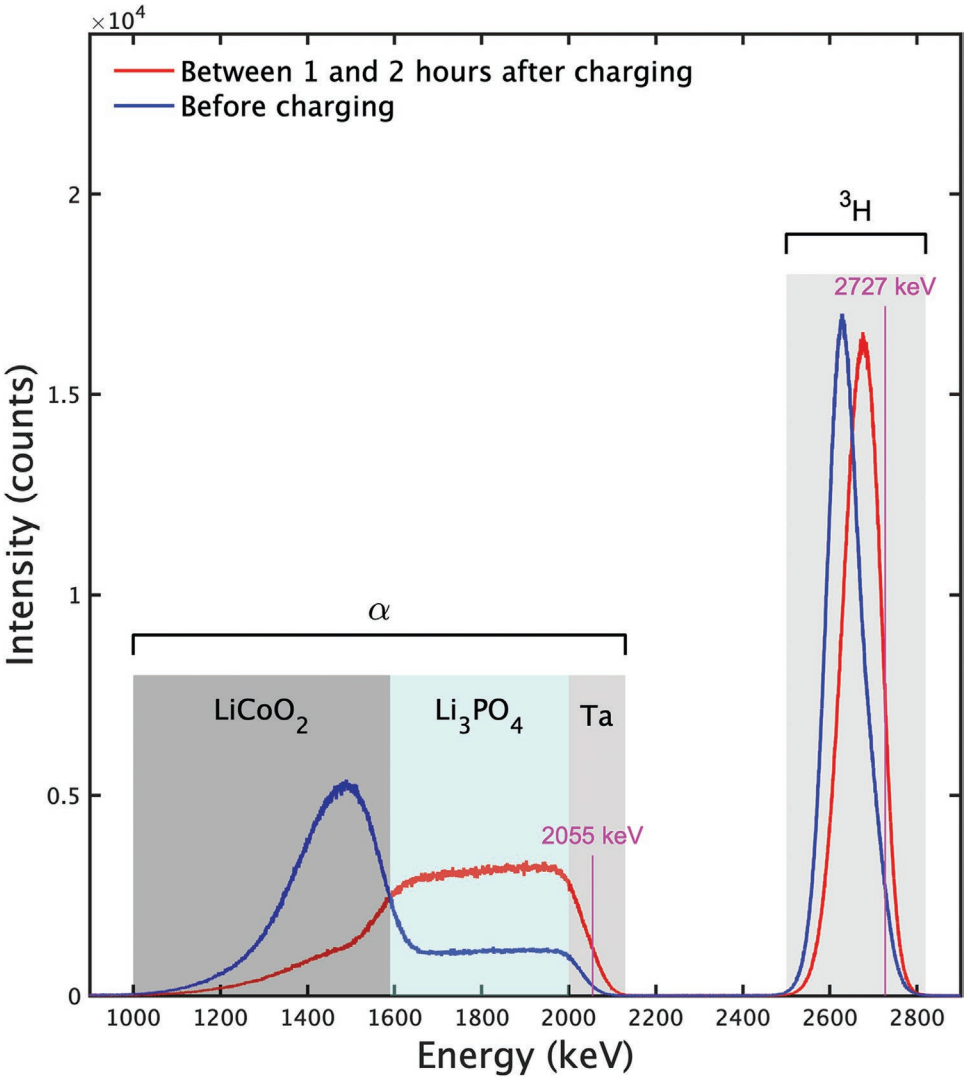

Figure 3. Comparative energy spectra obtained for an acquisition time 1 h. The blue and red curves show the spectra obtained for 1 h before charging and between 1 and 2 h after charging, respectively.

Figure 7d–f, respectively, represents changes in the number of lithium-6 ions as a function of position (column) in Figure 7a–c. As can be seen from Figure 7b–e, when lithium ions from the positive electrode, which is mostly lithium-6, move uniformly over the entire region of the solid electrolyte, the concentration of lithium-6 should be high in the solid electrolyte on the positive side. This is inconsistent with the experimental result, which has a much better fit with the simulated result of the selected area migration model. These results together strongly suggest that in the Li_3PO_4 solid electrolyte, lithium ions do not move uniformly across the entire electrolyte, but instead follow a limited pathway.

As can be seen from Table 2, the isotope ratio of the solid electrolyte after charging is 0.218. This ratio is established by the coexistence of a region with a natural abundance isotope (0.0759) and a region with an enriched lithium-6 isotope ratio (0.954). Therefore, the following equation should hold:

$$0.0759\times(1-R_t)+0.954\times R_t=0.218 \quad (1)$$

where R_t is the ratio of the region where the isotope ratio of lithium-6 is enriched, and $(1 - R_t)$ is the ratio of the region where the isotope ratio is the natural abundance. That is, the first term of the equation indicates the amount of naturally abundant lithium-6 in the region when the total number of lithium in the solid electrolyte is 1, and the second term of the equation represents the amount of lithium-6 in the region where lithium-6 is enriched when the total number of lithium in the solid electrolyte is 1. By solving Equation (1), R_t is calculated to be 0.162. Further research is needed to clarify which part of the solid electrolyte of the lithium ions is transporting to in relation to this value.

3. Conclusions

By utilizing the $^6Li(n,\alpha)^3H$ thermal neutron-induced nuclear reaction, with lithium-6 as a tracer, and a high-intensity thermal neutron beam from JRR-3, the transport of lithium ions in an

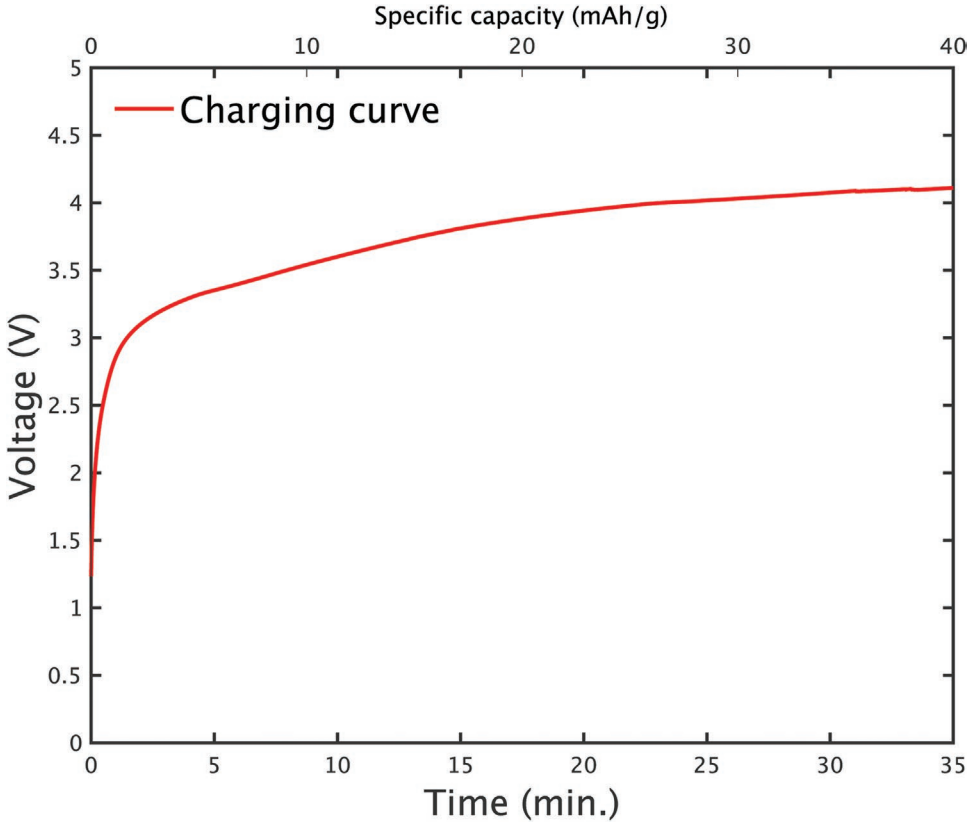

Figure 4. Charging curve showing the charging voltage as a function of time.

all-solid-state battery of Pt/$LiCoO_2$/Li_3PO_4/Ta during charging was tracked in near real time. From the observed transport, it is suggested that the transport of lithium ions in the Li_3PO_4 solid electrolyte occurs via the vacancy migration mechanism, and that the migration occurs over a limited area of the electrolyte. In this present study, the battery sample was exposed to atmosphere before experiments. However, it would be possible to analyze a battery sample without exposing it to atmosphere by using a small (portable) vacuum chamber equipped with a neutron window. Furthermore, although a thin film sample was used in this study, a sample with thick solid electrolyte could be analyzed by installing a detector in front of and behind the sample. Additionally, in future work, we plan to utilize the advantages of this analytical method to elucidate the transfer mechanisms of lithium ions in various other solid electrolyte systems. Such research will clarify whether there is a universal migration mechanism of lithium ions moving in solid electrolytes or whether competing processes are involved. Thus, tracking the transport of lithium ions in all-solid-state batteries could provide a spark in the research and development of next-generation battery technologies.

4. Experimental Section

Preparation of Lithium-6-Enriched $LiCoO_2$ Sputter Target: A standard $LiCoO_2$ sputter target was sintered using Li_2CO_3 and CoO as raw materials. The lithium-6 enriched one was similarly sintered from $^6Li_2CO_3$ and CoO. $^6Li_2CO_3$ was purchased from ISOTECH in the USA. The sintering was commercially performed by TOSHIMA Manufacturing Co., Ltd. in Japan.

Preparation of a Sample Battery: The structure of the battery used for experiments was consisted of a silicon substrate, a Pt current collector, a $LiCoO_2$ positive electrode (target thickness for deposition of 500 nm), a Li_3PO_4 solid electrolyte (1000 nm), and Ta as an equivalent negative electrode (27 nm), as referenced from the substrate side. Although the natural abundance of lithium-6 was 0.0759, the isotope ratio of lithium 6 in the cathode had been enriched up to 0.954. The battery was fabricated using RF sputtering, except for the Pt and Ta layers, which were deposited by DC sputtering. As a result, the crystallographic structure of the Pt, $LiCoO_2$, Ta layers were polycrystalline. In addition, the Li_3PO_4 layer was amorphous. The effective diameter of the battery sample was 45 mm.

Charging the Battery: As a power source for charging the battery, a Keithley model 2450 was used. The charge current and cutoff charging voltage were 250 μA and 4.2 V, respectively.

Charging or Discharging Rate: In the case of constant current charge/discharge measurements, the magnitude of the current that fully charged (or discharged) the theoretical capacity of the battery in 1 h was defined as 1C.

Vacuum Chamber for Experiments: A series of experiments were carried out by placing the battery in the center of a small cylindrical vacuum chamber with an inner diameter of 169 mm and an inner height of 110 mm. Beam windows were installed in the front and rear of the chamber, irradiating thermal neutrons with a size of 20 mm^2. The materials for the chamber and the windows were aluminum and zirconium, respectively. The thickness of the windows was 0.2 mm. The degree of vacuum in the chamber during the analysis was kept below 10^{-3} Pa.

Method for Lithium Depth Profiling Using $^6Li(n,\alpha)^3H$ Thermal Neutron-Induced Nuclear Reaction: When the lithium-containing sample was irradiated by a thermal neutron beam with an energy of 0.025 eV, the

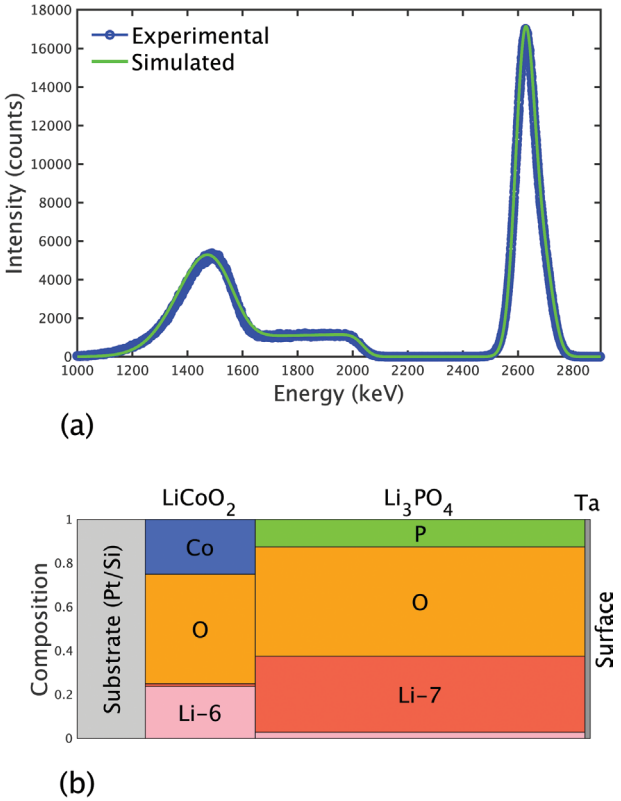

Figure 5. a) Analysis of energy spectra before charging using SIMNRA. b) Schematic of the depth profile of each element of each layer.

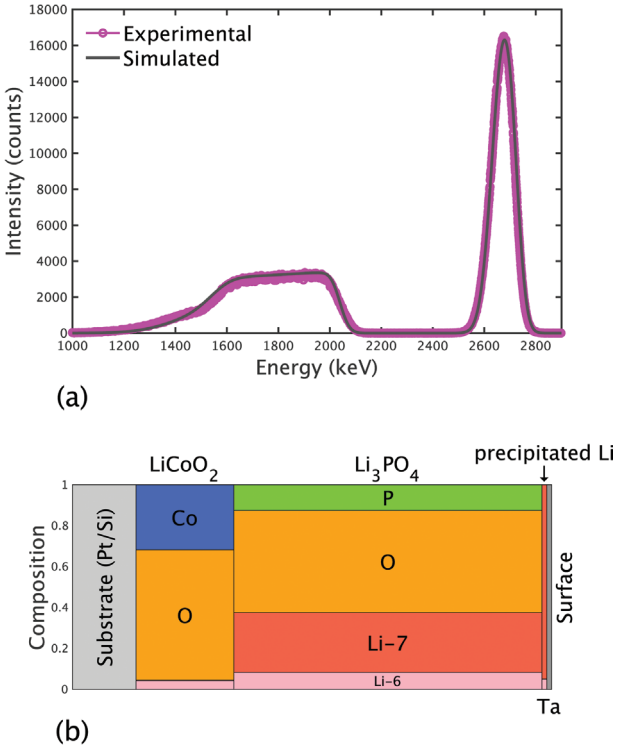

Figure 6. a) Analysis of energy spectra obtained between 1 and 2 h after charging using SIMNRA. b) Schematic of the depth profile of each element of each layer between 1 and 2 h after charging.

neutrons reacted with the lithium-6, following the nuclear reaction $^6Li + n \rightarrow \alpha$ (energy of particle immediately after the reaction: 2055 keV) + ^3H (2727 keV). Since the energy of the neutrons that caused the reaction was as low as 0.025 eV, the reaction was isotropic even in the laboratory system. In addition, the particles produced by the reaction lost energy until they exited the sample. Therefore, by analyzing the energies of the particles, the depth distribution of lithium in the sample could be obtained. Moreover, this method was a sort of light elemental analysis method using neutron-induced nuclear reaction called neutron depth profiling.

Spectra Acquisition System: To enable measurement without exposing the sample to the atmosphere after installing the sample battery in the chamber, a detector and a corresponding signal cable were installed in the chamber. In this series of experiments, the detector was installed at 150° to the neutron beam and the distance between the sample and the detector was 45 mm. The detector used was the Canberra PIPS detector (PD 50-11-300 AM). The output signal from the detector was amplified

Table 1. Numbers of atoms (ions) of each element cm^{-2} used in SIMNRA simulation to analyze the spectrum for 1 h before charging.

Before charging						
Element	$Li_{(1-x)}CoO_2$		Li_3PO_4		Ta(27 nm)	Total $^6Li+^7Li$
	Concentration [isotope ratio]	Numbers of atoms [10^{15} atoms cm^{-2}]	Concentration [isotope ratio]	Numbers of atoms [10^{15} atoms cm^{-2}]	Numbers of atoms [10^{15} atoms cm^{-2}]	Numbers of atoms [10^{15} atoms cm^{-2}]
^6Li	(0.954)	906.3[a]	(0.0759)	381.4[a]		1287.7[a]
^7Li	(0.046)	43.7[b]	(0.9241)	4643.6[b]		4687.3[b]
$^6Li+^7Li$	0.25	950.0[b]	0.375	5025.0[b]		5975.0[b]
O	0.5	1900.0[c]	0.5	6700.0[c]		
Co	0.25	950.0[c]				
P			0.125	1675.0[c]		
Ta					150	
Total	1	3800.0[d]	1	13 400.0[d]	150	5975.0[b]
Roughness[e] [10^{15} atoms cm^{-2}]		2600.0[a]		2600.0[a]		

[a]Measured values; [b]Values calculated from isotope ratio; [c]Values calculated from concentrations; [d]Values obtained by taking the sum; [e]Roughness: the nonuniformity of the film thickness deposited on the smooth substrate.

Table 2. Numbers of atoms (ions) of each element cm^{-2} used in SIMNRA simulation to analyze the spectrum measured for 1 h between 1 and 2 h after charging.

After charging								
Element	$Li_{(1-x)}CoO_2$		Li_3PO_4		Precipitated Li		Ta (27 nm)	Total $^6Li+^7Li$
	Concentration [isotope ratio]	Numbers of atoms [10^{15} atoms cm^{-2}]	Concentration [isotope ratio]	Numbers of atoms [10^{15} atoms cm^{-2}]	Concentration	Numbers of atoms [10^{15} atoms cm^{-2}]	Numbers of atoms [10^{15} atoms cm^{-2}]	Numbers of atoms [10^{15} atoms cm^{-2}]
^6Li	(0.954)	127.9[a)]	(0.0759)	1095.45[a,g)]	0.079	64.34[d)]		1287.7[c)]
^7Li	(0.046)	6.2[b)]	(0.9241)	3929.55[b,g)]	0.921	751.55[d)]		4678.3[c)]
$^6Li+^7Li$	0.045	134.1[b)]	0.375	5025.0[c)]	1	815.9[d)]		15 975.0[c)]
O	0.637	1900.0[c)]	0.5	6700.0[c)]				
Co	0.318	950.0[c)]						
P			0.125	1675.0[c)]				
Ta							150	
Total	1	2984.1[e)]	1	13 400.0[c)]	1	815.9[d)]	150	15 975.0[c)]
Roughness[f)] [10^{15} atoms cm^{-2}]		2600.0[c)]		2600.0[c)]				

[a)]Measured values; [b)]Values calculated from isotope ratio; [c)]Value assuming that the total amount of lithium is the same as before charging; [d)]Values calculated assuming that the total amounts of lithium-6 and lithium-7 are preserved before and after charging; [e)]Values obtained by taking the sum; [f)]Roughness: the nonuniformity of the film thickness deposited on the smooth substrate; [g)]Isotope ratio of lithium-6 in Li_3PO_4 solid electrolyte after charging: 0.218 (= 1095.45/5025.0).

by a charge-sensitive FET input preamplifier (Canberra model 2004), the signal was input to a Caen N6730B, and processed under the control of the Caen CoMPASS software.[30] With this configuration, the energy spectrum from the start of the measurement was displayed on the computer monitor. The Caen CoMPASS software had the ability to save spectral data at set time intervals, which allowed easy calculation of time changes in the spectrum.[30] In the present study, spectral data had been recorded with an interval of 1 min.

Statistical Analysis: Thermal neutron-induced nuclear reaction (energy) spectra were measured at 1-min intervals as mentioned before. As a result, the total yields of α-particles in each spectrum were constant within the statistical error. For this reason, the normalization

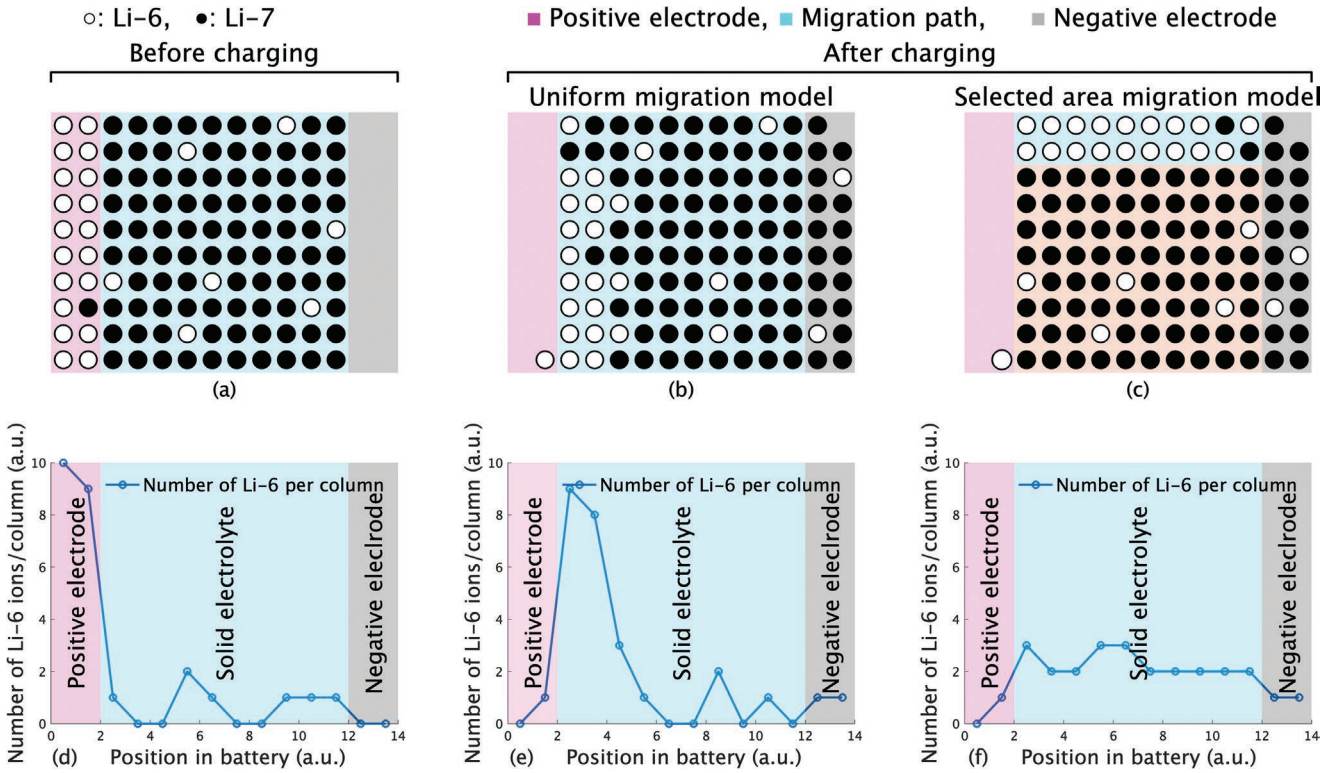

Figure 7. Migration path models in the Li_3PO_4 solid electrolyte. a) Initial (before charging) distribution of lithium-6 and lithium-7 ions (atoms), b) distribution of lithium-6 and lithium-7 ions (atoms) in the final state (after charging) when migrated by the uniform migration model, c) equivalent distribution for the selected area migration model. d–f) represent, respectively, changes in the number of lithium-6 ions as a function of position (column) in (a)–(c).

of the spectra was performed using the total yield of α particles for each spectrum. In addition, the total yields of ^{3}H particles in all spectra were equal to those of α particles within statistical error. All statistical analyses were performed using MATLAB for macOS (version 2022b; MathWorks, Natick, MA).

Supporting Information

Supporting Information is available from the Wiley Online Library or from the author.

Acknowledgements

The authors thank H. Matsue for his useful discussions in the experiments using JRR-3. This research was partially supported by Engineering Network Project at RIKEN; a Materials Processing Science project ("Materealize") of the Ministry of Education, Culture, Sports, Science and Technology, Japan (MEXT); a KAKENHI Grant-in-Aid for Scientific Research on Innovative Areas "Interface IONICS" (grant No. JP19H05813) from the Japan Society for the Promotion of Science (JSPS); and JST grant No. JPMJPF2016. This work was performed under the Shared Use Program of JAEA Facilities.

Conflict of Interest

The authors declare no conflict of interest.

Data Availability Statement

The data that support the findings of this study are available from the corresponding author upon reasonable request.

Keywords

all-solid-state lithium batteries, lithium transport, lithium-6 tracer, neutron depth profiling, real-time tracking, thermal neutron-induced nuclear reaction

Received: July 19, 2022
Revised: September 6, 2022
Published online: September 30, 2022

[1] T. Famprikis, P. Canepa, J. A. Dawson, M. S. Islam, C. Masquelier, *Nat. Mater.* **2019**, *18*, 1278.
[2] H. Wang, D. Ning, L. Wang, H. Li, Q. Li, M. Ge, J. Zou, S. Chen, H. Shao, Y. Lai, Y. Zhang, G. Xing, W. K. Pang, Y. Tang, *Small* **2022**, *18*, 2107491.
[3] M. Chen, Y. Zhang, G. Xing, S.-L. Chou, Y. Tang, *Energy Environ. Sci.* **2021**, *14*, 3323.
[4] S. Möller, T. Satoh, Y. Ishii, B. Teßmer, R. Guerdelli, T. Kamiya, K. Fujita, K. Suzuki, Y. Kato, H.-D. Wiemhöfer, K. Mima, M. Finsterbusch, *Batteries* **2021**, *7*, 41.
[5] V. Mathayan, K. Morita, B. Tsuchiya, R. Ye, M. Baba, D. Primetzhofer, *Mater. Today Energy* **2021**, *21*, 100844.
[6] V. Mathayan, K. Morita, B. Tsuchiya, R. Ye, M. Baba, M. V. Moro, D. Primetzhofer, *J. Appl. Phys.* **2021**, *130*, 125306.
[7] K. Morita, K. B. Tsuchiya, R. Ye, H. Tsuchida, T. Majima, *Solid State Ion* **2021**, *370*, 115730.
[8] V. Mathayan, M. V. Moro, K. Morita, B. Tsuchiya, R. Ye, M. Baba, D. Primetzhofer, *Appl. Phys. Lett.* **2020**, *117*, 023902.
[9] K. Morita, B. Tsuchiya, R. Ye, H. Tsuchida, T. Majima, *Nucl. Instrum. Methods. Phys. Res. B.* **2020**, *478*, 249.
[10] B. Tsuchiya, J. Ohnishi, Y. Sasaki, T. Yamamoto, M. Motoyama, Y. Iriyama, K. Morita, *Adv. Mater. Interfaces* **2019**, *6*, 1900100.
[11] B. Tsuchiya, K. Morita, S. Nagata, T. Kato, Y. Iriyama, H. Tsuchida, T. Majima, *Surf. Interface Anal.* **2014**, *46*, 1187.
[12] I. Tomandl, J. Vacil, T. Kobayashi, Y. M. Sierra, V. Hnatowicz, V. Lavreniev, P. Horak, G. Ceccio, A. Cannavo, M. Baba, R. Ye, *Radiat. Eff. Defects Solids* **2020**, *479*, 249.
[13] D. L. Danilov, C. Chen, M. Jiang, R.-A. Eichel, P. H. L. Notten, *Radiat. Eff. Defects Solids* **2020**, *175*, 367.
[14] J. Vacik, I. Tomandl, V. Hnatowicz, P. Horak, A. Cannavo, G. Ceccio, D. Fink, T. Kobayashi, R. Ye, M. Baba, *AIP Conf. Proc.* **2019**, *2160*, 030005.
[15] Q. Li, T. Yi, X. Wang, H. Pan, *Nano Energy* **2019**, *63*, 103895.
[16] C. Wang, Y. Gong, J. Dai, L. Zhang, H. Xie, G. Pastel, B. Liu, E. Wachsman, H. Wang, L. Hu, *J. Am. Chem. Soc.* **2017**, *139*, 14257.
[17] J. F. M. Oudenhoven, F. Labohm, M. Mulder, R. A. H. Niessen, F. M. Mulder, P. H. L. Notten, *Adv. Mater.* **2011**, *23*, 4103.
[18] A. Sagara, K. Kamada, S. Yamaguchi, *Nucl. Instrum. Methods. Phys. Res. B.* **1988**, *1088*, 465.
[19] W. Assmann, H. Huber, C.h. Steinhausen, M. Dobler, H. Glückler, A. Weidinger, *Nucl. Instrum. Methods. Phys. Res. B.* **1994**, *89*, 131.
[20] R. G. Downing, G. P. Lamaze, *Neutron News* **1993**, *4*, 15.
[21] R. G. Downing, R. F. Fleming, J. K. Langland, D. H. Vincent, *Nucl. Instrum. Methods. Phys. Res. B.* **1983**, *218*, 47.
[22] Y. Kawabata, M. Suzuki, H. Kikuchi, M. Sano, *J. Nucl. Sci. Technol.* **1993**, *30*, 1050.
[23] Japan Atomic Energy Agency, About JRR-3, https://jrr3.jaea.go.jp/jrr3e/1/11.htm (accessed: July 2022).
[24] H. Matsue, https://jrr3.jaea.go.jp/images/202107.pdf (accessed: July 2022).
[25] Y. Kato, S. Hori, T. Saito, K. Suzuki, M. Hirayama, A. Mitsui, M. Yonemura, H. Iba, R. Kanno, *Nat. Energy* **2016**, *1*, 16030.
[26] W. Li, Y. Ando, E. Minamitani, S. Watanabe, *J. Chem. Phys.* **2017**, *147*, 214106.
[27] N. Kuwata, N. Iwagami, Y. Tanji, Y. Matsuda, J. Kawamura, *J. Electrochem. Soc.* **2010**, *157*, A521.
[28] M. Mayer, *AIP Conf. Proc.* **1999**, *475*, 541.
[29] M. Mayer, SIMNRA User's Guide, https://mam.home.ipp.mpg.de/SIMNRA-Users-Guide.pdf (accessed: July 2022).
[30] Caen, Manual of data acquisition software for Caen digitizer, https://www.caen.it/products/compass/ (accessed: July 2022).